# High-spectral-resolution absorption measurements with free-electron lasers using ghost spectroscopy

Yishai Klein,[1,*] Alok K. Tripathi,[1,*] Edward Strizhevsky,[1] Flavio Capotondi,[2] Dario De Angelis,[2] Luca Giannessi,[2,3] Matteo Pancaldi,[2] Emanuele Pedersoli,[2] Kevin C. Prince,[2,4] Or Sefi,[1] Young Yong Kim,[5,6] Ivan A. Vartanyants,[5] and Sharon Shwartz[1,†]

[1]*Physics Department and Institute of Nanotechnology and Advanced Materials, Bar Ilan University, Ramat Gan, 52900, Israel*
[2]*Elettra-Sincrotrone Trieste, Strada Statale 14-km 163.5, Basovizza, 34149, Trieste, Italy*
[3]*Istituto Nazionale di Fisica Nucleare, Laboratori Nazionali di Frascati, Via Enrico Fermi 54, 00044 Frascati, Roma, Italy*
[4]*Department of Chemistry and Biotechnology, School of Science, Computing and Engineering Technology, Swinburne University of Technology, Melbourne 3122, VIC, Australia*
[5]*Deutsches Elektronen-Synchrotron DESY, Notkestrasse 85, 22607 Hamburg, Germany*
[6]*European XFEL, Holzkoppel 4, 22869 Schenefeld, Germany*

(Received 22 December 2022; accepted 29 March 2023; published 5 May 2023)

We demonstrate a simple and robust high-resolution ghost spectroscopy approach for x-ray and extreme ultraviolet transient absorption spectroscopy at free-electron laser sources. To retrieve the sample response, our approach requires only an online spectrometer before the sample and a downstream bucket detector. We validate the method by measuring the absorption spectrum of silicon, silicon carbide, and silicon nitride membranes in the vicinity of the silicon $L_{2,3}$ edge and by comparing the results with standard techniques for absorption measurements. Moreover, we show that ghost spectroscopy allows the high-resolution reconstruction of the sample spectral response to optical pumps using a coarse energy scan with self-amplified spontaneous emission radiation.

DOI: 10.1103/PhysRevA.107.053503

## I. INTRODUCTION

X-ray and extreme ultraviolet (XUV) free-electron lasers (FELs) are very powerful and bright sources that enable measurements of ultrafast phenomena in a broad range of processes [1,2]. Short wavelength spectroscopy is widely used for the determination of the electronic structure of materials and provides element specific information on the charge and spin structures as well as bonding configurations, which are important for understanding the functionality of materials [3]. When performed at FELs, x-ray spectroscopy can provide information on the dynamics of the processes by using pump-probe schemes, where the short FEL pulse probes a process that is triggered by an external stimulus, which can be provided either by an optical laser or by the FEL itself. By varying the delay between the pump and the probe pulses, full information on the dynamics of the electronic response of the sample can be recorded [4].

There are basically two common strategies for the measurement of high-resolution absorption spectra. The first is to use narrowband (quasimonochromatic) radiation and to measure the total transmitted intensity after the sample (or the emitted fluorescence, which is often proportional to the absorption). With this approach the spectrum of the sample response is reconstructed by scanning the photon energy of the input radiation and registering the intensities measured by the detector for each input photon energy. The monochromaticity of the pulse is obtained either by using a monochromator [5] or by using one of the seeding schemes depending on the wavelength of the radiation [6–8]. A second strategy is implemented when the radiation has a broadband spectrum ($\Delta\lambda/\lambda \sim 1\%$ or more). In this case, the spectrum of the transmitted radiation is compared with the spectrum of the input beam before the sample [9] and it is absolutely necessary to know the spectrum before and after the sample with high precision and fidelity. The energy resolution of the first approach depends on the spectral bandwidth of the input radiation whereas, in the second case, it is determined by the resolving power of the spectrometers that are used for the spectral measurements.

The advantages of the broad bandwidth pulse strategy are the possibility to measure broad ranges of spectra without scanning the central emission wavelength, and the availability of higher flux. Therefore, this approach can be significantly faster than the narrow bandwidth approach and useful for the measurement of low-efficiency processes. However since broad bandwidth FEL pulses are generated usually by using the process of self-amplified spontaneous emission (SASE) [10,11], the pulse energy and the spectra vary randomly from one shot to another. Thus, it is necessary to measure the spectra before and after the sample on a shot-to-shot basis. While single-shot spectrometers have been developed [12–16], the simultaneous application of two such spectrometers for these measurements is challenging, time consuming, and expensive. Furthermore, signal-to-noise (SNR) requirements impose a

*These authors contributed equally to this work.
†sharon.shwartz@biu.ac.il

 

limitation on the minimum number of photons that must be detected for the reconstruction of the spectra, which leads to stringent requirements for the input flux and limits the dynamical range of absorption magnitudes that can be measured. Thus, the range of samples that can be measured with standard methods is limited. Finally, while with a narrowband pulse the absorption can be inferred from the measurement of the fluorescence yield, which is often proportional to the absorbance, in the broadband scheme it is not possible since the comparison between the two spectrometers is required. Thus, the scheme can only be applied to transmissive samples (or for samples that allow the measurement of the photocurrent), which strongly limits the choice of materials that can be studied at FELs.

From the above it is clear that the choice of experimental method depends on a range of factors: the available light source, which may be SASE only; the spectrometers available; the desired energy and temporal resolution for time-resolved experiments; and the time available for measurement, which is very often strictly limited. An alternative strategy to perform absorption spectroscopy with FEL radiation that overcomes the challenges of the above-described approaches is ghost spectroscopy (GS), which is a form of correlation spectroscopy. Being a method that relies on multiplexed measurements rather than direct measurements it presents a number of advantages, with respect to the duration of the experiment, the simplicity of the setup, and the resolution of the measurement [17]. This technique has been demonstrated with radiation in the optical range [18–21] and recently with soft x rays using SASE pulses generated by FELs [22–24]. In addition, a closely related approach has been used recently with hard x rays to measure simultaneously the unoccupied and occupied electronic states of the atom by using two spectrometers and correlation [25]. The concept of GS is also closely related to ghost imaging (GI) [26], which has been successfully applied with laboratory [27,28], synchrotron [29–33], and FEL [34] x-ray sources.

The key parameter for GS is the variation of the spectral features from one shot to another. GS indeed exploits the stochastic nature of the SASE pulse spectra, i.e., the random shot-to-shot variation of the multispike spectra. Within this method, the spectrum of radiation impinging on the sample is measured and correlated on a shot-by-shot basis with the measured intensity of a single-pixel detector (usually a photodiode) that has no spectral resolution and is mounted after the sample. The measured intensity at this detector is proportional to the integral of the product of the spectrum of the input pulse and the spectral dependence of the transmission of the sample, i.e., its transmission function. Therefore, for each pulse, if the correlation between the input spectrum and the transmission function of the sample is high, the detector measures high intensity. Conversely, if the correlation is low, it measures low intensity. By repeating this procedure for many input pulses with different spectral distributions, it is possible to reconstruct the absorption spectrum of the sample [17,35]. The term ghost here refers to the fact that neither of the detectors can provide the spectrum, in direct analogy to GI, where the pixelated detector is blind to the object and the bucket detector does not provide spatial information [26–34].

Here, we present a simple and robust approach for GS in the XUV photon-energy range that requires only one spectrometer in front of the sample and a photodiode placed behind it. By replacing the downstream spectrometer with a photodiode, our approach greatly simplifies the experimental setup for absorption measurements with SASE FELs. At most facilities only the spectrometer before the sample is permanently installed so our method eliminates the need for the precise realignment of the downstream spectrometer, which is typically required with the standard broadband approach. This saves considerable time and effort and minimizes systematic errors that can arise from imprecise alignment. Our approach thus enables more complex and precise experiments to be performed at FELs, with minimal setup and alignment requirements. By directly comparing the measurement times and the spectral resolution of the GS case with that obtained by setting the FEL emission in SASE and seeded configurations, we demonstrate that GS is an efficient strategy to perform absorption spectroscopy at FELs. Furthermore, we extend the method and demonstrate its applicability for pump-probe measurements. As with the static measurements, the transient approach provides very highenergy resolution with a significantly reduced number of measurements.

## II. METHODS

### A. Experimental setup and radiation properties

We conducted the experiment at the DiProI (Diffraction and Projection Imaging) end station [36,37] using the double-cascade FEL source FEL-2 of the FERMI user facility located in Trieste, Italy [38]. This source can produce either SASE FEL radiation [39] or seeded FEL pulses [7,38] depending on the setting parameters. To demonstrate our approach for GS, we tuned the SASE pulse central energy in the photon-energy range between 99 and 106 eV for the measurements of the Si $L_{2,3}$ edges. The radiation produced by the source was focused by a set of bendable Kirkpatrick-Baez mirrors [40] to a spot size of about $500 \times 600$ $\mu m^2$ at the sample position; the polarization was circular and the pulse duration was estimated to be about 250 fs. The repetition rate was 50 Hz. The setup of our experiment is presented in Fig. 1. The online spectrometer was the pulse-resolved energy spectrometer transparent and online (PRESTO) [16], which is mounted at FERMI after the undulators and before the end stations. In the PRESTO spectrometer, a grating delivers most of the radiation in zeroth order (97%) to the end stations, while the weaker first order of the grating is used to measure the spectrum of each pulse.

The spectrometer resolution in the working energy range is $\Delta\lambda/\lambda \sim 5 \times 10^{-5}$ [16], corresponding to an energy resolution of about 5 meV at 100 eV. Examples of the spectral distribution of the FEL pulses in the SASE configuration and the average over 8000 shots are presented in Fig. 2(a). In our experiment, we mounted the sample in the direct beam and measured three different membranes of silicon (Si), silicon nitride ($Si_3N_4$), and silicon carbide (SiC), 200 nm thick, provided by Norcada. The average energy per pulse at the sample plane was $18.5 \pm 3$ $\mu$J, corresponding to a deposited energy density per pulse of $6 \pm 1$ mJ/cm$^2$, which is well below the typical damage threshold of the samples [41]. For the

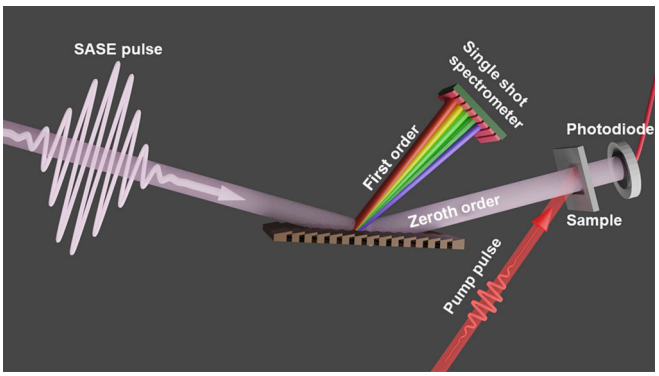


FIG. 1. GS experimental scheme. The input SASE radiation is split by a grating installed at the PRESTO instrument. The first order is used as a reference that is measured by a single-shot spectrometer mounted before the sample. The zeroth order irradiates the sample and the transmitted radiation after the sample is measured by a photodiode. The pump is an optical laser that is tuned to excite the electrons form the valence band to the conduction band.

detector with no energy resolution, we used a $10 \times 10$ mm$^2$ photodiode with an yttrium aluminum garnet (YAG) scintillator screen to convert the FEL radiation into optical radiation. The detector was mounted at about 500 mm downstream from the sample. At the detector position, due to the beam divergence, the FEL spot size was about $3 \times 4$ mm$^2$.

For the pump-probe measurements the optical excitations were triggered by a pump laser at 3.1 eV (400 nm) with a pulse duration of about 100 fs, beam dimensions of $700 \times 670$ μm$^2$, and fluence of 8.5 mJ/cm$^2$. In the experiment, we measured various delays from −5 to 150 ps and the angle between pump radiation and the sample was ∼5°.

For the GS measurements and photon energies in the range of 99–106 eV we varied the central photon energy of the SASE radiation with a step size of 250 meV. At each of the SASE photon energies we measured 2000 shots and the SASE bandwidth spans a range of 500 meV [full width at half maximum (FWHM), as can be seen in Fig. 2(a)].

To account for the dependence of the beamline transmission on the photon energy, we compared the total intensities of the spectrometer and the photodiode without the sample every time we changed the central photon energy of SASE emission. For the GS measurements and photon energies in the range of 99–106 eV we varied the central photon energy of the SASE radiation with a step size of 250 meV. At each of the SASE photon energies we measured 2000 shots and the SASE bandwidth spans a range of 500 meV [FWHM, as can be seen in Fig. 2(a)].

To account for the dependence of the beamline transmission on the photon energy, we compared the total intensities of the spectrometer and the photodiode without the sample every time we changed the central photon energy of SASE emission. We eliminated the background noise of the camera of the spectrometer by subtracting the dark reference images collected without FEL illumination.

Since GS is based on the intensity correlation between the spectral features recorded on the spectrometer and the intensity fluctuation recorded by the single-pixel detector placed behind the sample, it was important to ensure a highly linear correlation between the total recorded intensities on the two detectors in the absence of the sample. To compare the correlation quality between the two devices, we define the relative error "$R$" for each $i$th pulse as

$$R_i = \frac{I_{S_i}/\langle I_s\rangle - I_{P_i}/\langle I_P\rangle}{I_{P_i}/\langle I_P\rangle}, \tag{1}$$

where $I_{S_i}$ and $I_{P_i}$ are the total intensity of the $i$th shot, measured by the spectrometer and the photodiode, respectively, and $\langle\cdots\rangle$ represents an average over all pulses.

We found that the typical standard deviation of the relative error distribution of our experimental setup was about 7.5%. A typical distribution of the relative intensity errors between the two detectors, for an ensemble of 36 000 FEL pulses at a variety of energies within our scan range, is presented in Fig. 2(b). The main contributions to the error distribution are (1) The contamination of the high harmonics generated by the source that is not suppressed by the optics before the spectrometer; (2) the shot-to-shot beam pointing jitter, which is important

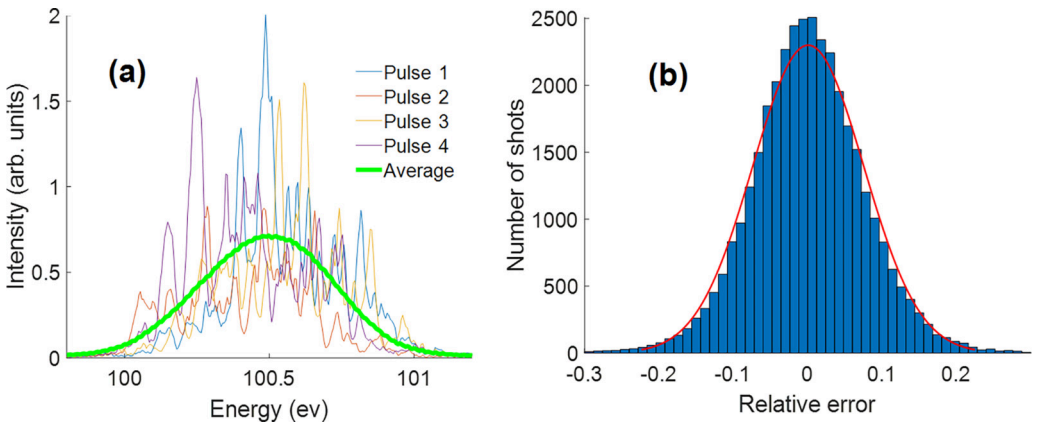


FIG. 2. (a) Energy distribution of the SASE pulses measured by the online spectrometer, when the central photon energy is set at 100.5 eV. The thinner lines are the spectra of four individual pulses and the thick green line is the average over 8000 pulses. (b) The relative error distribution between the total intensities at the spectrometer and the photodiode averaged over 36 000 pulses (blue bins). The red line is the Gaussian fit and the standard deviation is 7.5%.

since the spectrometer and the bucket detector detect slightly different portions of the beam; (3) the presence of off-axis spurious radiations that can impose spatial dependence of the spectral components; (4) the impact of the finite dimensions of the beamline mirrors, which may clip the beam; (5) shot noise. However, as we show in the next section, the error distribution we observed is sufficiently small for the GS reconstruction.

### B. Seeded radiation and synchrotron measurements

To compare the method of GS with conventional scanning approaches, we used FERMI FEL radiation in the seeded configuration, where the FEL pulses are generated using a ∼100 fs (FWHM) external laser pulse in the ultraviolet range from 4.7 to 4.9 eV to trigger the FEL amplification process [7,38]. By using a harmonic upshift factor of 21 the output radiation spans a photon energy from 99 to 103 eV. As shown in [42] the seeded FEL generated at FERMI is close to the Fourier limit and the pulse duration is estimated to be about 30 fs [43]. In this experiment the normalized FWHM bandwidth is $\Delta\lambda/\lambda = 1 \times 10^{-3}$, equivalent to an energy resolution of about 100 meV at 100 eV. Therefore, we scanned the photon energy of the seeded radiation with step sizes of 75 meV and measured the transmission of the silicon membrane near the $L_{2,3}$ edges in a range comparable to the GS measurement. The transmission of the membrane at each photon energy was calculated as the ratio between the average pulse energy detected by the photodiode and the average total pulse energy detected by the spectrometer. In addition, we performed the same procedure for the SASE scanning: in this case, almost all the electron bunch participates in the FEL process, resulting in a FEL pulse duration of about 250 fs (FWHM).

To validate our method, we compared the spectra we measured at FERMI with spectral measurements of the same samples at the BEAR beamline at the Elettra synchrotron [44]. In this latter case, the spectral sample transmission at each energy point is simply the average intensity measured after the sample divided by the input average intensity.

### C. GS reconstruction procedure

To reconstruct the ghost spectrum for each SASE central energy, we exploited the following reconstruction procedure. We represent the intensities of the $N$ pulses measured by the photodiode by a vector $\mathbf{T}$ (test data). The spectra of the pulses are represented by the matrix $\mathbf{A}$ for which every row is the spectral distribution of a single pulse (reference data). We represent the transmission function of the sample as a vector $\mathbf{x}$, and thus the vector $\mathbf{T}$ is equal to the product of the matrix $\mathbf{A}$ and the vector $\mathbf{x}$:

$$\mathbf{Ax} = \mathbf{T}. \tag{2}$$

In GS experiments, we measure the vector $\mathbf{T}$ and the matrix $\mathbf{A}$. We are interested in solving Eq. (2) for the vector $\mathbf{x}$ using the compressive sensing (CS) algorithm of "total variation minimization by augmented Lagrangian and alternating direction algorithms" (TVAL3) [45]. However, this algorithm works well only when the width of the average spectrum is much broader than the spectral range under investigation. Unfortunately, the SASE bandwidth in our case was narrower than the total measured spectral range. To overcome this challenge, we used the following procedure: first we normalized the matrix of the raw data by the average SASE distributions [for example, for the central photon energy at 100.5 eV we used the green line in Fig. 2(a)]:

$$\mathbf{B}_{i,j} = \frac{\mathbf{A}_{i,j}}{\frac{1}{N}\sum_{k=1}^{N}\mathbf{A}_{k,j}}. \tag{3}$$

Next, we normalized the reference and the test data by the pulse energy of each pulse:

$$\mathbf{C}_{i,j} = \frac{\mathbf{B}_{i,j}}{\frac{1}{M}\sum_{k=1}^{M}\mathbf{B}_{i,k}}, \quad \mathbf{T'}_i = \frac{\mathbf{T}_i}{\frac{1}{M}\sum_{k=1}^{M}\mathbf{B}_{i,k}}. \tag{4}$$

By using this procedure, we can replace Eq. (2) with a new equation,

$$\mathbf{Cx'} = \mathbf{T'}, \tag{5}$$

where the matrix representing the different energy distributions in each pulse is now the effective matrix $\mathbf{C}$ where the envelope is normalized and the shot-to-shot intensity variations are filtered out.

Next, we used the TVAL3 algorithm to solve Eq. (5). The basic idea of TVAL3 is to recognize that the gradients of the measured spectra can be represented by a sparse vector. The vector $\mathbf{x'}$ is reconstructed by minimizing the augmented Lagrangian,

$$\min_{\mathbf{x'}} \sum_{j=1}^{M} \|D_j\mathbf{x'}\|_2 + \frac{\mu}{2}\|\mathbf{Cx'} - \mathbf{T'}\|_2^2 \text{ subject to } \mathbf{x'} \geqslant 0, \tag{6}$$

with respect to the $l_2$ norm. In Eq. (6), $D_j\mathbf{x'}$ is the $j$th component of the discrete gradient of the vector $\mathbf{x'}$, and $\mu$ is the penalty parameter of the model (here we set $\mu = 2^6$). We note that for the reconstruction of the transmission function of the sample (the vector $\mathbf{x}$) the vector $\mathbf{x'}$ that we obtained by using the described algorithm is renormalized to obtain

$$\mathbf{x}_j = \frac{\mathbf{x'}_j}{\frac{1}{N}\sum_{k=1}^{N}\mathbf{A}_{k,j}}. \tag{7}$$

The mathematical justification for this procedure is described in the Appendix.

After we reconstructed separately the absorption spectrum for each SASE central energy of the SASE scan, we merged all the absorption spectra to create the spectrum of the sample. At this point, the number of data points is much larger than the number of points corresponding to the GS resolution since, as we will discuss below, the resolution of GS is determined by the width of the individual spectral spikes [46], which are broader than the resolution of the spectrometer. Therefore, the final step was to bin the points to obtain a bin size equal to the spike width.

## III. RESULTS AND DISCUSSION

### A. Ghost spectroscopy results

The GS results for the three samples are presented in Fig. 3. The blue dots are the GS reconstructions, and the magenta

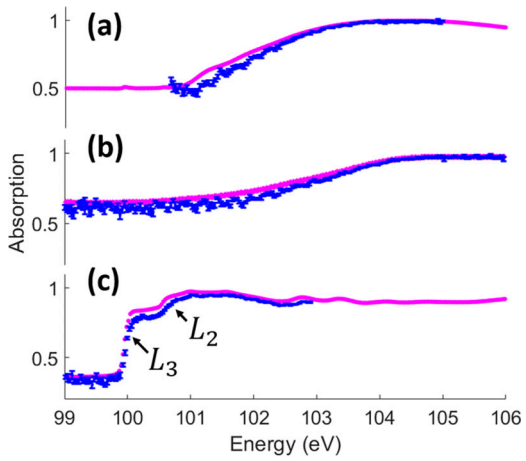


FIG. 3. GS $L_{2,3}$ edge spectra of (a) silicon carbide (SiC), (b) silicon nitride ($Si_3N_4$), and (c) silicon (Si). The blue dots are the GS results, and the magenta (light gray) dots are the results obtained by the monochromatic synchrotron measurements.

(light gray) dots are the results of the synchrotron monochromatic scan that we used to validate our method. It is clear from Fig. 3 that the agreement between the GS reconstruction using the FEL and the synchrotron measurements is very good. We conclude that the energetic chemical shift of the Si $L_{2,3}$ resonances in the three different samples due to the different Si bonding is well monitored by GS reconstruction. Furthermore, the contribution of the spin orbit splitting to the $L_{2,3}$ edge is clearly visible in the absorption spectrum of crystalline Si near 100.2 eV of the silicon membrane [47] and indicates that the GS resolution is much better than the width of each of the edges, which is around 100 meV. The agreement with the spectra measured by the synchrotron also indicates that the resolution of the GS is close to the resolution of the synchrotron, which is about 30 meV.

To compare the GS method, the scanning of the seeded radiation method, and the scanning of the SASE radiation method, we plot the spectra measured by these three different approaches for the Si sample in Fig. 4(a).

While the photon-energy resolutions of the seeded and the SASE radiation are simply determined by the spectral width of their pulse envelopes, the resolution of GS is mostly related to the spectral width of each individual spike of the SASE spectrum. More precisely, we estimated the resolution of the three methods by calculating the FWHM of the autocorrelation function and by dividing it by $\sqrt{2}$. This protocol provides the spectral width of the individual spikes for GS [46] and the spectral width for the SASE and the seeded radiations. The autocorrelation function values of the SASE pulses averaged over 2000 pulses are the black dots in Fig. 4(b). The magenta line is a fit of the sum of two Gaussian curves. The two curves represent the spectral width of the SASE pulse and the width of the spectral spikes. Using the same procedure, we present the autocorrelation function of the seeded pulses in Fig. 4(c), where the narrower Gaussian corresponds to the spectral width of the seeded pulse. In Fig. 4(d) we present these three Gaussian fits that correspond to the energy resolutions of the SASE (green dashed line), seeded (red dotted line), and GS (blue solid line), respectively. It is important to note that the spectral width of the SASE radiation determines

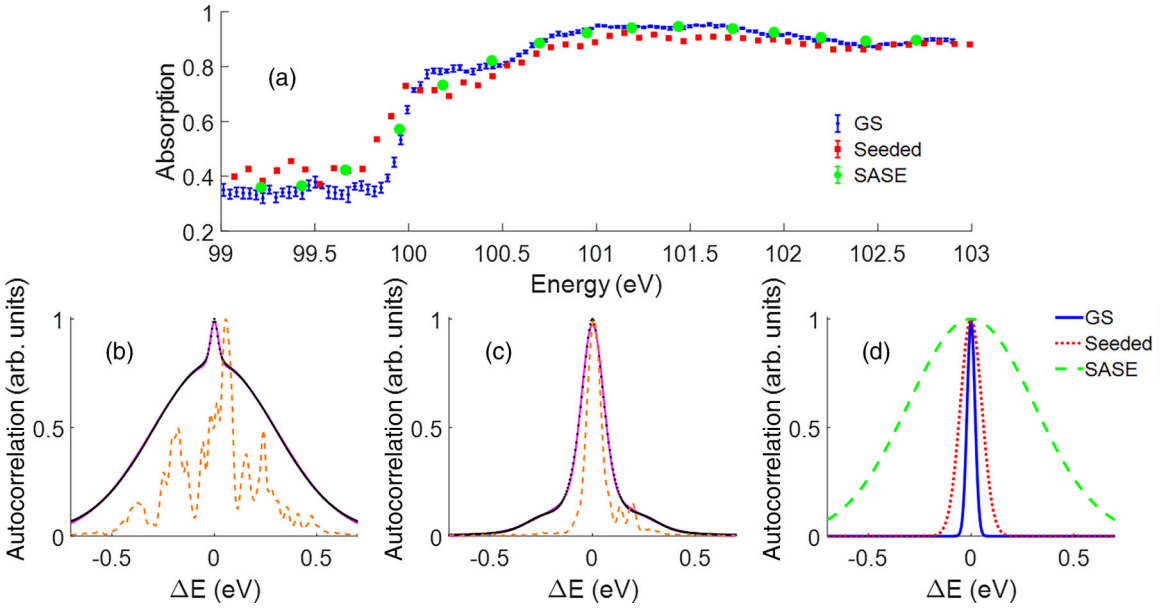


FIG. 4. (a) Comparison of the GS results (blue dots) with the spectrum collected by scanning FEL pulses generated in the seeded (red squares) and the SASE (green circle) configurations. The statistical error of the SASE and seeded measurements was about 1% and too small to be seen. (b), (c) Averaged autocorrelation function of SASE and seeded radiation, respectively. The black dots are the values of the autocorrelation function that are calculated from the measured data and the magenta line is a fit of the sum of two Gaussians. The orange dashed line is an example of a single-shot spectrum. (d) Gaussian fits from the autocorrelation function, which we used for the calculation of the resolutions of the three methods. The resolutions are 500, 75, and 35 meV for SASE, seeded, and GS methods, respectively.

the spectral range of the GS reconstruction at each of the SASE central photon-energy steps.

The widths of the Gaussian profiles reported in Fig. 4(d) indicate clearly that GS provides a higher resolution than the one reached in seeded mode and much higher than the SASE case, but with a number of scans that is equal to the number of scanning points used in SASE mode. For the same spectral range from 99 to 103 eV, with GS we used 15 steps and the resolution was 35 meV; with the SASE radiation we also used 15 steps, but the resolution was only 500 meV; and with the seeded radiation we used 51 steps and the resolution was 75 meV.

In principle, it is possible to increase the spectral resolution in seeded mode by increasing the duration of the optical laser seeding pulse, but at the expense of increasing the number of step points per scan to map a given spectral interval. For GS the trade-off between the resolution and the number of step points is lifted.

### B. Number of pulses required for the reconstruction of the spectrum

In the previous section, we showed that GS requires a smaller number of step points per scan compared with the seeded radiation to cover the same spectral range. However, the measurement time also depends on the number of shots required to stabilize the result at each energy point, which is different between the GS and the seeded beam scans.

A seeded FEL behaves indeed as a laserlike source [48] and has stable output wavelength and power. An ideal measurement of the input wavelength and of the pulse energy before and after the sample would be sufficient to measure one sample of the absorption spectrum with a single FEL shot. In practice, the noise associated to the energy detection as well as the loss due to photon transport reduces the correlation between the two energy measurements, and even the acquisition of a single spectral sample requires averaging over a number of shots to improve the signal-to-noise ratio.

Conversely, in GS the spectrum reconstruction requires a set of spectral acquisitions. The single measurement provides only a fraction of the spectral information at each frequency sample, but simultaneously on the samples distributed over the broad range of frequencies corresponding to the SASE pulse bandwidth. The SASE spectrum has the structure of spikes of random amplitude and distribution; the fluctuation statistics of each bin in the measured spectrum depends therefore on the width of the bin itself. The highest achievable spectral resolution with GS corresponds to spectral bins separated by a width comparable to the spike spectral width. Increasing the bin size reduces the spectral resolution, but improves the statistics collected at each shot and requires a lower number of shots to ensure the convergence of the analysis. It has been shown for GI that the number of iterations scales as the number of the pixels in the reconstructed image [49] and we expect a similar dependence for GS. To test this important aspect, we first compared the dependence of the quality of the absorption spectrum measurements on the number of shots for the GS and the seeded radiation.

To quantify the quality of the reconstructed spectrum we consider the synchrotron data as the accurate reference absorption spectrum and define the mean absolute error $\langle\varepsilon\rangle$ as

$$\langle\varepsilon\rangle = \frac{1}{M}\sum_{j=1}^{M}|x_j - g_j|, \tag{8}$$

where $x_j$ is the $j$th point in the reconstructed spectrum (by GS or seeded), $g_j$ is the $j$th point in the ground truth which is the synchrotron measurement, and $M$ is the number of points.

We plot $\langle\varepsilon\rangle$ as a function of the number of shots for the GS (blue dots) and for the seeded radiation (red squares) in Fig. 5(a). The comparisons (in addition to the synchrotron measurement as a reference) for various numbers of shots per scanning point are shown in Figs. 5(c)–5(h). In our experiment the spectrum we reconstructed by GS was slightly closer to the synchrotron results than the spectrum obtained with the seeded radiation. The smallest $\langle\varepsilon\rangle$ for GS is around 0.035 and for the seeded radiation it is 0.055. This comparison indicates that GS can provide high-quality spectra with a number of pulses per point that is comparable to the seeded radiation scan.

The small difference between the GS results and the seeded radiation results may indicate a systematic error and thus it is difficult to infer from Fig. 5(a) which method converges to its best value faster. We therefore defined the "convergence factor," $C_F$, similarly to the above definition of the $\langle\varepsilon\rangle$ as

$$\boldsymbol{C}_F = \frac{1}{M}\sum_{j=1}^{M}|x_j - b_j|, \tag{9}$$

where now $b_j$ represents the best value for GS and for the seeded mode separately, which is the $j$th point in the reconstructed spectrum using 2000 pulses for GS and seeded radiation. For this comparison we bin the GS dataset to 35 meV, corresponding to the value used in the plots 5(a) and 5(c)–5(f) (blue-solid line) and 75 meV to match the resolution of the seeded radiation (blue dashed line). In Fig. 5(b) we show the $C_F$ for the GS and for the seeded radiation scans as a function of the number of pulses per scanning point in the three cases. The convergence of GS is comparable to the convergence of the seeded mode at equal resolution and slower when the resolution of the GS is higher, requiring more shots to reach a similar $C_F$. This implies that when the resolution is equal the required number of shots per data point with the GS and with the seeded radiation are comparable; hence the measurement time with GS is shorter than with the seeded radiation.

Another interesting result from this comparison is that even with a small number of 300 pulses per scanning point, the quality of the reconstructed spectrum obtained by GS was sufficient to resolve the main features of the Si $L_{2,3}$ edge spectrum. In our experiment the repetition rate was 50 Hz and the number of scanning points for the GS was 15, which implies that the measurement time was 90 s.

### C. Compression factor dependence

As discussed in the previous sections the resolution of GS is determined by the average width of the single SASE

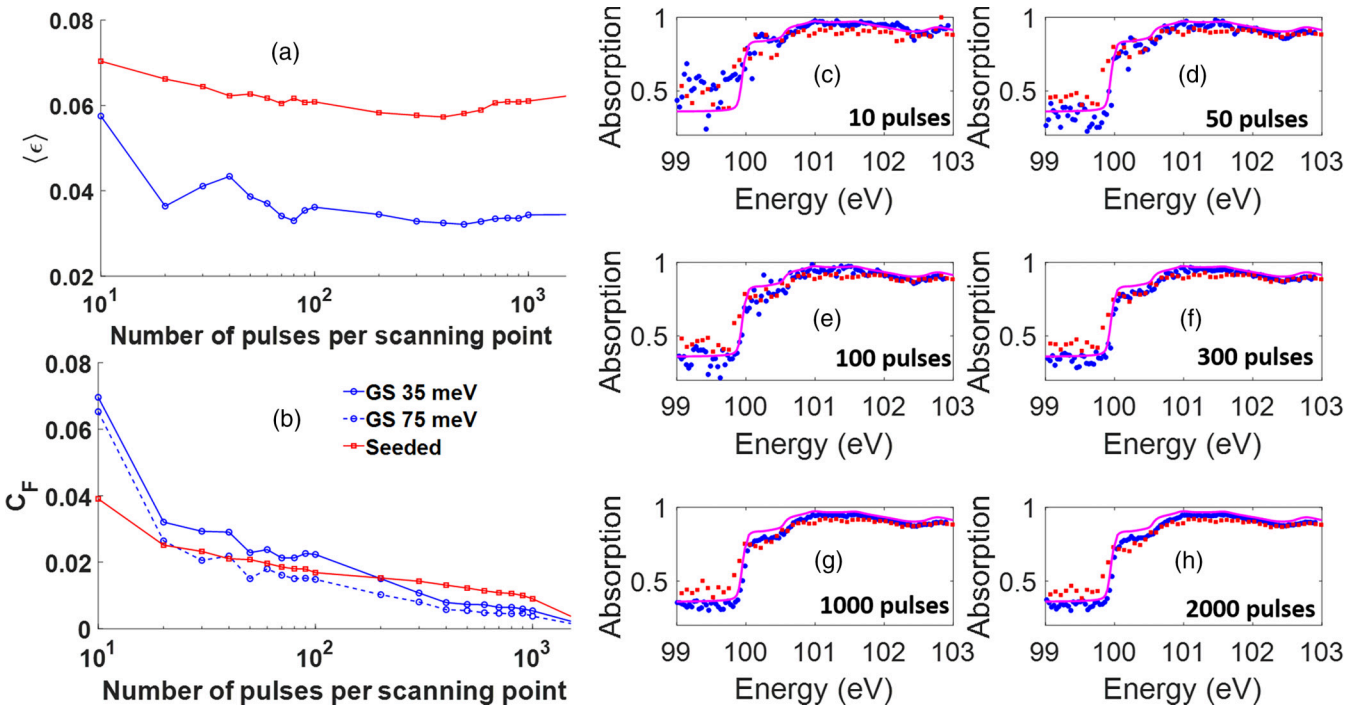


FIG. 5. (a) The mean absolute error and (b) convergence factor of the reconstructed spectrum of the silicon membrane as a function of the number of pulses per scanning point for the GS (blue dots) and the seeded radiation (red squares). (c)–(h) The reconstructed spectrum results with GS (blue circles) and with seeded radiation (red squares) compared to the synchrotron measurements (magenta line) as a guide using (c) 10, (d) 50, (e) 100, (f) 300, (g) 1000, and (h) 2000 pulses per scanning point.

spectral spikes. The main parameter that we can use to control the spike width is the electron bunch compression factor [50]. To compress the electron bunch, we used a magnetic double chicane located inside the acceleration section of the FERMI source. A typical compression is used at FERMI to increase the peak current up to about 650 A [51]. The compressor can be tuned to further compress the beam to reach a higher peak current. In Fig. 6(a) we show typical energy pulse spectra for a modestly compressed electron beam (blue line) and for a highly compressed electron bunch (purple dots), respectively. The two graphs clearly show that the primary spectral features are different in the two regimes, with more and wider spikes for a highly compressed electron beam.

To demonstrate this dependence more quantitatively we show in Fig. 6(b) the spike width (calculated by the FWHM of the autocorrelation Gaussians divided by $\sqrt{2}$) as a function of the peak current. The results indicate that the spectral spike's width grows linearly with the compression of the electron beam, which is in agreement with the previous study [50]. In our experiment the peak current was about 900 A, corresponding to a spectral width of 35 meV, while for higher current (i.e., 2150 A) the width is about 60 meV. The conclusion from this discussion is that by controlling the compression factor it is possible to control the spectral resolution of our approach. It is important to note, however, that the compression also affects the coherence and the pulse duration of the SASE emission [50,52].

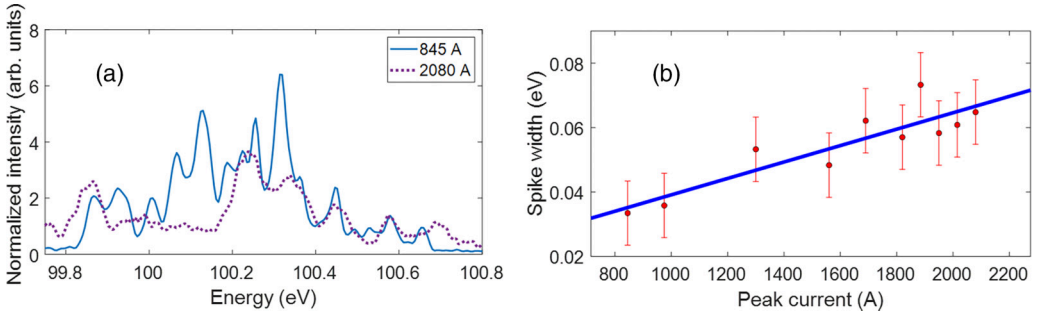


FIG. 6. (a) Typical single-shot FEL pulse spectra for 845 A (blue solid line) and 2080 A (purple dotted line) of the peak current of the electron bunch. (b) Spike width as a function of the peak current. The vertical error bars represent the uncertainty caused by the spectrometer resolution and the fitting procedure.

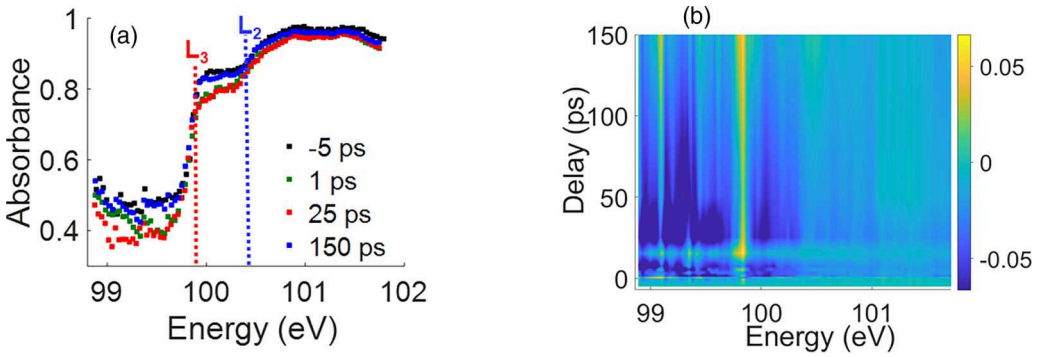


FIG. 7. Photoinduced absorption variation in the silicon membrane: (a) XUV absorption spectra at various pump delays. (b) Differential absorption map.

### D. Pump-probe measurements

To demonstrate the ability to measure photoinduced variation in the $L$-edge absorption spectrum with GS we plot the spectra at $-5$ ps (before the arrival of the optical pulse), 1, 25, and 150 ps delays between the optical pump and the XUV pulses in Fig. 7(a).

The largest differences between the photoexcited and the ground state spectrum can be clearly seen at a delay of 1 and 25 ps for photon energies that are slightly above the $L_3$ edge (from 99.8 to 100.3 eV) and below the edges.

For a better understanding of the dynamics of the photoinduced effects we numerically calculated the differential absorbance by subtracting absorbance at $-5$ ps, where the probe arrives before the pump, from the absorbance at a particular delay and plotted the results in Fig. 7(b). The color maps were produced by interpolation with the measured data from $-5$ to 150 ps. Inspecting Fig. 7(b), we see several different behaviors in the dynamics of the variation of the spectrum. To interpret Fig. 7(b), we recall that the $L_3$ and the $L_2$ edges are at about 99.8 and 100.3 eV, respectively, and that they correspond to excitations from the $2p$ states (the upper- and lower-spin states, respectively) to the bottom of the conduction band. We first explain the results of Fig. 7(b) by considering the dynamics of the charge carriers. Since the photon energy of the optical laser is 3.1 eV, it excites electrons from the valence band to the direct valley (the $\Gamma$ point) of the conduction band. Thus, immediately after the excitation of the electrons, the number of unoccupied states at the $\Gamma$ point is reduced, and holes are created in the valence band. At delays longer than the optical pulse duration, the charge carriers relax from their excited state, first by electron-electron scattering and at later times (several ps) by electron-phonon scattering [53]. As a result of the relaxation processes, the electrons lose energy and temporarily occupy states at energies lower than the $\Gamma$ point in the conduction band and inside the gap (i.e., isolated impurity states); they eventually relax back to the valence band by Auger recombination after several tens of ps [53]. Thus, we expect the charge carrier dynamics to lead to a reduction in the absorption near 99.8 eV and to an increase in the absorption below 98.7 eV. Since the transition from the $2p$ level to the $\Gamma$ point is dipole forbidden [53] and since the temporal resolution in our experiment was $\sim$350 fs, we observed only the slower relaxation dynamics. The relaxation from the $\Gamma$ point to the bottom of the conduction band and to the gap states is clearly seen in the form of the reduction in the absorption in the energy range from 98.8 to 99.8 eV and from 99.9 to 101.7 eV from a delay of 0 ps to a delay of 25 ps and again from a delay of 25–150 ps.

However, there are several interesting features in Fig. 7(b) that cannot be explained by considering only excitations and relaxations of charge carriers. These are the increased absorption in the narrow area between 99.8 and 99.9 eV and the trend of the variation at delays between 1 and 7 ps. The discrepancy between the observations and the explanation based on charge carrier dynamics indicates a possible photoinduced modification of the band structure of the silicon and related structural changes.

If these photoinduced variations exist, they should lead to shifts of the edges and to further variations of the absorbance of the sample mainly near the edges. We therefore plot the delay dependence of positions of the edges in Figs. 8(b)–8(d).

We estimate the edge position by numerically calculating the derivative of the absorbance spectrum. This derivative peaks at the edges as can be seen in the examples for 0 and 25 ps delays shown in Fig. 8(a). This figure clearly shows that the $L_3$ edge shifts from $99.79 \pm 0.035$ to $99.87 \pm 0.035$ eV after 25 ps from the optical stimulus. The same behavior is observed at the $L_2$ edge lying at $100.30 \pm 0.035$ and $100.40 \pm 0.035$ eV, at 0 and 25 ps delay, respectively. The other two peaks observed in Fig. 8(a) below the $L$ edges can be attributed to impurity states in the Si gap.

The full dynamics of the $L_{2,3}$ edges are reported in Figs. 8(b) and 8(c). We can see that the $L_3$ and the $L_2$ states shift to lower photon energies from 3 to 5 ps. From 5 to 7 ps both edges returned to their original positions. Again from 7 to 25 ps both the edges exhibit negative shifts and then they return to their original position after 150 ps. The largest shift of the $L_3$ edge is $-0.08$ eV and the largest shift of the $L_2$ edge is $-0.10$ eV, occurring at 25 ps delay. While obviously we did not measure sufficient delays in the region near the largest deviation, the results are consistent with the theory that predicts that a few ps after the excitations the conduction band is shifted toward the valence band [54] and with pertinent publications [55]. This can explain the positive variation of the absorption just below the edge, which we see in Fig. 7(b) since the shift of the conduction band and the

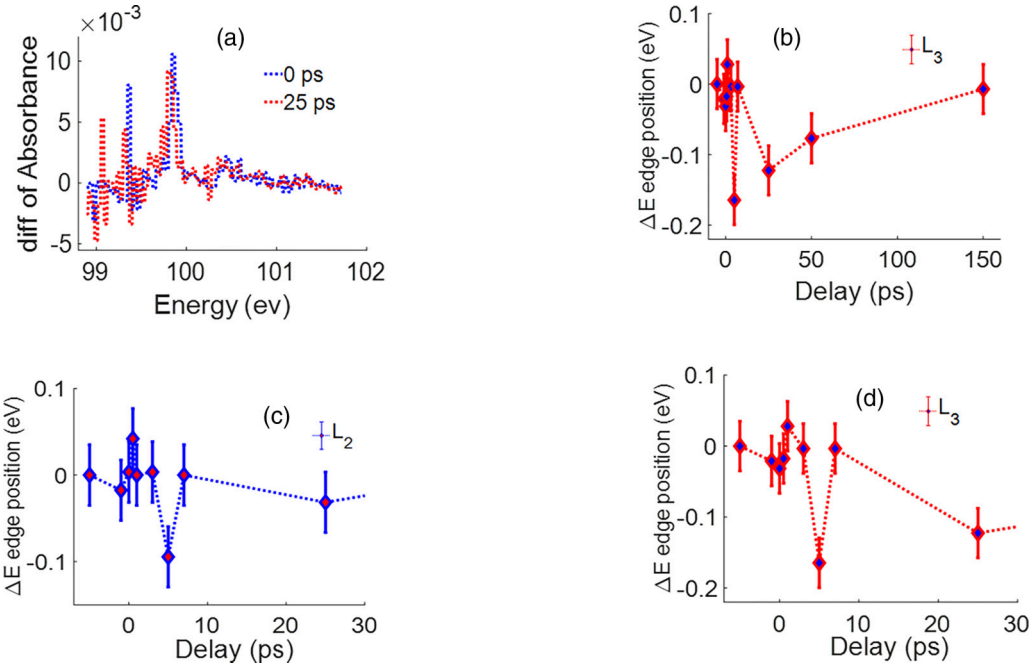


FIG. 8. Variation of the edge position: (a) derivatives of the absorption spectra of at 0 and 25 ps delays. (b) The change of the position of the $L_3$ edge with the delays. (c), (d) Enlarged view of the change of the position of the $L_2$ and $L_3$ edges, respectively, from –5 to 25 ps.

corresponding change in the density of states near the bottom of the band can lead to this positive variation. The shift at a delay of several ps can be attributed to electron-phonon interaction and the shift at longer delays to the change in the structure of the silicon that leads to the variation in the band gap. The nonmonotonic behavior has to be investigated in detail and suggests that several processes can impact the variation of the band gap, for example, the temperature and pressure of the hot charge carriers. Since the spectral resolution in our experiment was 35 meV, the small positive shifts we see in Fig. 8 are smaller than our experimental precision.

Comparing our results with pertinent work on transient XUV spectroscopy in silicon, we note that Leone and colleagues [53] reported a detailed study of the transient photoinduced variation of the absorption spectrum by using a high harmonic generation source as the probe and with optical pumps at several wavelengths. The time resolution in their experiment was higher than ours; thus they could monitor the dynamics on the 100 fs scale. The intensity of the optical laser they used was about an order of magnitude weaker than the intensity we used, and their spectral resolution (500 meV) was lower than ours. Most of our results agree with that work and with the theoretical models they suggested. The main differences are due to the higher intensity in the present work, which led to more pronounced variations in the band structure. Since we had a better spectral resolution, we observed several structures they did not observe (the edge shifts, in particular), but they all agree with the theory.

In another work, Beye *et al.* [55] reported a photoinduced phase transition with the optical fluence of 250 mJ/cm$^2$, which is about just 30 times higher than the fluence used here. In their experiment they also used a 400 nm laser, but they measured the XUV fluorescence. The shift of 80 meV for $L_3$ and 200 meV for $L_2$ which we observed when the optical fluence was 8.5 mJ/cm$^2$ suggests that a photoinduced phase transition can occur only if the fluence dependence of the variation in the band structure is highly nonlinear. This is because the band gap is about 1.1 eV.

## IV. CONCLUSION

In this paper we have demonstrated the implementation of GS for an XUV FEL with an online spectrometer in front of the sample and a photodiode after the sample. The experimental setup is simple and can provide high spectral resolution with SASE FELs without additional spectrometers after the sample or monochromatizating the input beam. We have validated the quality of the absorption spectrum measurements by comparing to more conventional methods and found that the spectral resolution is comparable to the resolution of scans with seeded radiation. Our results indicate that the measurement time with GS can be significantly shorter than the measurement time with seeded radiation. From our analysis we conclude that the reduction in the measurement time is comparable to the ratio of the average spectral width of the SASE regime to the spectral width of the seeded one at a comparable spectral resolution. We emphasize that we do not expect that GS will be always faster than scans with quasi-monochromatic radiation and stress that the exact conditions depend on various details such as the specific properties of the FEL and the sparsity of the absorption spectrum. The spectral resolution of the GS method is determined by the lower resolution of either the width of spectral autocorrelation of the SASE radiation or the resolution of the spectrometer. Our work therefore calls for the improvement of the resolution of single-shot spectrometers and for the reduction of the spectral width of the SASE spikes.

The results of the pump-probe experiment that we present demonstrate the applicability of ghost spectroscopy for transient absorption spectroscopy and for the study of photoinduced effects with high-photon-energy FELs. The method can lead to a novel and efficient procedure for transient spectroscopy at high photon energies. It is important to note that the time resolution in our method is limited by the pulse duration of the input pump and probe pulses, while the spectral resolution is limited by the width of the spectral spikes. This trade-off between the time and the spectral resolution, that find their optimum for Fourier transform limited pulses, has to be considered when designing measurements with ghost spectroscopy.

## ACKNOWLEDGMENTS

Y.K. gratefully acknowledges the support of the Ministry of Science & Technologies, Israel. This work is supported by the Israel Science Foundation (ISF) (Grant No. 201/17).

## APPENDIX: RECONSTRUCTION PROCEDURE FOR GHOST SPECTROSCOPY WHEN USING SASE FLUCTUATIONS

In the following paragraphs we provide further details on the derivation of the equations we used for the reconstruction of the absorption spectrum from the measured data in the experiment of ghost spectroscopy (GS).

To reconstruct the absorption spectrum of the object is we need to solve Eq. (2) of the main text:

$$\mathbf{T} = \mathbf{A}\mathbf{x}, \tag{A1}$$

where $\mathbf{T}$ is a vector that includes the intensities of $N$ pulses measured by the photodiode, $\mathbf{x}$ is a $P$-length vector representing the transmission function of the sample, and $\mathbf{A}$ is a $N \times M$ matrix where every row represents the spectral distribution of a single pulse. However, the raw data from the measurements include not just the spectral response of the sample but also the constant envelope of the SASE fluctuations [the green line shown in Fig. 2(a) of the main text] and the shot-to-shot intensity instability, which is a general property of FELs. It is therefore necessary to eliminate the information that is not directly related to the sample. The idea of the procedure below is to exploit an auxiliary matrix $\mathbf{C}$ that contains the spectral information without the SASE envelope and to normalize the shot-to-shot intensity variation.

We recall that we can represent each element of the matrix $\mathbf{A}$ as

$$\mathbf{A}_{i,j} = a_i \mathrm{A}^*_{i,j} \mathrm{F}_j, \tag{A2}$$

where the spectral envelope is the $M$-length vector $\mathbf{F}$ and the shot-to-shot intensity variation is represented by $a_i$ for each $i$th shot. $\mathrm{A}^*_{i,j}$ is a random value from a normal distribution, i.e., $\mathrm{A}^*_{i,j} \sim N(\mu, \sigma^2)$. By inserting Eq. (A2) into Eq. (A1) we get

$$\mathbf{T}_i = \sum_{j=1}^{M} \mathrm{A}_{i,j}\mathrm{x}_j = \sum_{j=1}^{M} a_i \mathrm{A}^*_{i,j}\mathrm{F}_j\mathrm{x}_j = \frac{a_i}{a}\sum_{j=1}^{M} \mathrm{A}^*_{i,j} a\mathrm{F}_j\mathrm{x}_j \tag{A3}$$

where $a$ is defined as $a = \frac{1}{N}\sum_{i=1}^{N} a_i$. To use the matrix for the reconstruction of the absorption spectrum we define the new matrix and vectors as

$$\mathrm{x}'_j = a\mathrm{F}_j\mathrm{x}_j, \quad \mathrm{B}_{i,j} = \frac{a_i}{a}\mathrm{A}^*_{i,j} = \frac{\mathrm{A}_{i,j}}{a\mathrm{F}_j}, \tag{A4}$$

and Eq. (A3) can be transformed to

$$\mathbf{T}_i = \sum_{j=1}^{P} \mathrm{A}'_{i,j}\mathrm{x}'_j \tag{A5}$$

which is equivalent to $\mathbf{T} = \mathbf{B}\mathbf{x}'$.

The matrix $\mathbf{B}$ contains the data of the spectral distribution of the input pulses normalized by the average spectral envelope of the raw measurements.

Assuming $\mathrm{A}^*_{i,j} \sim N(1, \sigma^2)$ and $a_i \sim N(a, \sigma^2)$, the envelope $a\mathrm{F}$ can be calculated by averaging over all the raw pulses:

$$\frac{1}{N}\sum_{i=1}^{N} \mathrm{A}_{i,j} = \frac{1}{N}\sum_{i=1}^{N} a_i \mathrm{A}^*_{i,j}\mathrm{F}_j = a\mathrm{F}_j \tag{A6}$$

Thus, the matrix $\mathbf{B}$ is related to the matrix $\mathbf{A}$ by

$$\mathbf{B}_{i,j} = \frac{\mathbf{A}_{i,j}}{a\mathbf{F}_j} = \frac{\mathbf{A}_{i,j}}{\frac{1}{N}\sum_{k=1}^{N}\mathbf{A}_{k,j}}, \tag{A7}$$

which is Eq. (3) of the main text.

To address the second challenge of the shot-to-shot intensity variation we normalized each measurement $\mathbf{T}_i$ by the value $a_i$ (and for convenience we multiply also by a constant factor $\frac{a}{M}$):

$$\boldsymbol{T}'_i = \frac{a}{P}\frac{\boldsymbol{T}_i}{a_i}. \tag{A8}$$

Using Eq. (A5) we can write

$$\boldsymbol{T}'_i = \frac{a}{M}\frac{1}{a_i}\sum_{j=1}^{M} B_{i,j} \tag{A9}$$

and

$$\mathbf{C}_{i,j} = \frac{a}{M}\frac{B_{i,j}}{a_i}. \tag{A10}$$

This leads to

$$\boldsymbol{T}'_i = \sum_{j=1}^{M} \mathrm{C}_{i,j}\mathrm{x}'_j \quad \text{or} \quad \mathbf{T}' = \mathbf{C}\mathbf{x}'. \tag{A11}$$

which is Eq. (5) of the main text. The matrix $\mathbf{C}$ contains spectral data that we used for the reconstruction of the transmission function of the object. They are separated from the envelope of the measured spectra and normalized to have equal pulse energy. The factor $a_i$ is calculated by

$$\begin{aligned}\frac{a}{M}\sum_{j=1}^{M} B_{i,j} &= \frac{1}{P}\sum_{j=1}^{M}\frac{\mathrm{A}_{i,j}}{\mathrm{F}_j} = \frac{1}{M}\sum_{j=1}^{M}\frac{a_i A^*_{i,j}F_j}{F_j} \\ &= \frac{1}{M}\sum_{j=1}^{M} a_i A^*_{i,j} = a_i\frac{1}{M}\sum_{j=1}^{M} A^*_{i,j} = a_i.\end{aligned} \tag{A12}$$

The vector $\mathbf{T}'$ and the matrix $\mathbf{C}$ are related to the vector $\mathbf{T}$ and the matrix $\mathbf{B}$ by the relations

$$\mathbf{T}_i^{'} = \frac{a}{M}\frac{T_i}{a_i} = \frac{a}{M}\frac{\mathrm{T_i}}{\frac{a}{M}\sum_{k=1}^{M}\mathrm{B}_{i,k}} = \frac{\mathbf{T}_i}{\sum_{k=1}^{M}\mathbf{B}_{i,k}} \quad \text{and}$$

$$\mathbf{C}_{i,j} = \frac{a}{M}\frac{B_{i,j}}{a_i} = \frac{\mathbf{B}_{i,j}}{\sum_{k=1}^{M}\mathbf{B}_{i,k}}, \tag{A13}$$

which lead to Eq. (4) of the main text. By using the definition of $\mathbf{x}'$ from Eq. (A4) we can find the actual transmission by using the relation

$$\mathbf{x}_j = \frac{\mathbf{x}'_j}{a\mathbf{F}_j} = \frac{\mathbf{x}'_j}{\frac{1}{N}\sum_{k=1}^{N}\mathbf{A}_{k,j}}, \tag{A14}$$

which leads to Eq. (7) of the main text.


[1] N. Huang, H. Deng, B. Liu, D. Wang, and Z. Zhao, Features and futures of x-ray free-electron lasers, Innovation **2**, 100097 (2021).

[2] C. Pellegrini, The development of XFELs, Nat. Rev. Phys. **2**, 330 (2020).

[3] P. Sedigh Rahimabadi, M. Khodaei, and K. R. Koswattage, Review on applications of synchrotron-based x-ray techniques in materials characterization, X-Ray Spectrom. **49**, 348 (2020).

[4] M. Maiuri, M. Garavelli, and G. Cerullo, Ultrafast spectroscopy: State of the art and open challenges, J. Am. Chem. Soc. **142**, 3 (2020).

[5] Y. Obara, H. Ito, T. Ito, N. Kurahashi, S. Thürmer, H. Tanaka, T. Katayama, T. Togashi, S. Owada, Y.-i. Yamamoto, S. Karashima, J. Nishitani, M. Yabashi, T. Suzuki, and K. Misawa, Femtosecond time-resolved x-ray absorption spectroscopy of anatase $TiO_2$ nanoparticles using XFEL, Struct. Dyn. **4**, 044033 (2017).

[6] S. Ackermann, A. Azima, S. Bajt, J. Bödewadt, F. Curbis, H. Dachraoui, H. Delsim-Hashemi, M. Drescher, S. Düsterer, B. Faatz *et al.*, Generation of Coherent 19- and 38-nm Radiation at a Free-Electron Laser Directly Seeded at 38 nm, Phys. Rev. Lett. **111**, 114801 (2013).

[7] E. Allaria, R. Appio, L. Badano, W. A. Barletta, S. Bassanese, S. G. Biedron, A. Borga, E. Busetto, D. Castronovo, P. Cinquegrana *et al.*, Highly coherent and stable pulses from the FERMI seeded free-electron laser in the extreme ultraviolet, Nat. Photonics **6**, 699 (2012).

[8] D. Xiang, E. Colby, M. Dunning, S. Gilevich, C. Hast, K. Jobe, D. McCormick, J. Nelson, T. O. Raubenheimer, K. Soong *et al.*, Demonstration of the Echo-Enabled Harmonic Generation Technique for Short-Wavelength Seeded Free Electron Lasers, Phys. Rev. Lett. **105**, 114801 (2010).

[9] G. Brenner, S. Dziarzhytski, P. S. Miedema, B. Rösner, C. David, and M. Beye, Normalized single-shot x-ray absorption spectroscopy at a free-electron laser, Opt. Lett. **44**, 2157 (2019).

[10] E. L. Saldin, E. V. Schneidmiller, and M. V. Yurkov, *The Physics of Free Electron Lasers* (Springer Science & Business Media, Berlin, 1999).

[11] S. V. Milton, E. Gluskin, N. D. Arnold, C. Benson, W. Berg, S. G. Biedron, M. Borland, Y.-C. Chae, R. J. Dejus, P. K. Denhartog *et al.*, Exponential gain and saturation of a self-amplified spontaneous emission free-electron laser, Science **292**, 2037 (2001).

[12] N. Kujala, W. Freund, J. Liu, A. Koch, T. Falk, M. Planas, F. Dietrich, J. Laksman, T. Maltezopoulos, J. Risch *et al.*, Hard x-ray single-shot spectrometer at the European x-ray free-electron laser, Rev. Sci. Instrum. **91**, 103101 (2020).

[13] J. Rehanek, M. Makita, P. Wiegand, P. Heimgartner, C. Pradervand, G. Seniutinas, U. Flechsig, V. Thominet, C. W. Schneider, A. R. Fernandez *et al.*, The hard x-ray photon single-shot spectrometer of SwissFEL—initial characterization, J. Instrum. **12**, P05024 (2017).

[14] Y. Inubushi, I. Inoue, J. Kim, A. Nishihara, S. Matsuyama, H. Yumoto, T. Koyama, K. Tono, H. Ohashi, K. Yamauchi *et al.*, Measurement of the x-ray spectrum of a free electron laser with a wide-range high-resolution single-shot spectrometer, Appl. Sci. **7**, 584 (2017).

[15] J. Rehanek, C. J. Milne, J. Szlachetko, J. Czapla-Masztafiak, J. Schneider, T. Huthwelker, C. N. Borca, R. Wetter, L. Patthey, and P. Juranic, A compact and versatile tender x-ray single-shot spectrometer for online XFEL diagnostics, J. Synchrotron Radiat. **25**, 16 (2018).

[16] C. Svetina, D. Cocco, N. Mahne, L. Raimondi, E. Ferrari, and M. Zangrando, PRESTO, the on-line photon energy spectrometer at FERMI: Design, features and commissioning results, J. Synchrotron Radiat. **23**, 35 (2016).

[17] T. J. Lane and D. Ratner, What are the advantages of ghost imaging? Multiplexing for x-ray and electron imaging, Opt. Express **28**, 5898 (2020).

[18] P. Janassek, S. Blumenstein, and W. Elsäßer, Ghost Spectroscopy with Classical Thermal Light Emitted by a Superluminescent Diode, Phys. Rev. Appl. **9**, 021001 (2018).

[19] P. Janassek, A. Herdt, S. Blumenstein, and W. Elsäßer, Ghost spectroscopy with classical correlated amplified spontaneous emission photons emitted by an erbium-doped fiber amplifier, Appl. Sci. **8**, 1896 (2018).

[20] C. Amiot, P. Ryczkowski, A. T. Friberg, J. M. Dudley, and G. Genty, Supercontinuum spectral-domain ghost imaging, Opt. Lett. **43**, 5025 (2018).

[21] S. Rabi, S. Meir, R. Dror, H. Duadi, F. Baldini, F. Chiavaioli, and M. Fridman, Spectral ghost imaging for ultrafast spectroscopy, IEEE Photonics J. **14**, 1 (2022).

[22] T. Driver, S. Li, E. G. Champenois, J. Duris, D. Ratner, T. J. Lane, P. Rosenberger, A. Al-Haddad, V. Averbukh, T. Barnard *et al.*, Attosecond transient absorption spooktroscopy: A ghost imaging approach to ultrafast absorption spectroscopy, Phys. Chem. Chem. Phys. **22**, 2704 (2020).

[23] S. Li, T. Driver, O. Alexander, B. Cooper, D. Garratt, A. Marinelli, J. P. Cryan, and J. P. Marangos, Time-resolved pump-probe spectroscopy with spectral domain ghost imaging, Faraday Discuss. **228**, 488 (2021).

[24] K. Li, J. Laksman, T. Mazza, G. Doumy, D. Koulentianos, A. Picchiotti, S. Serkez, N. Rohringer, M. Ilchen, M. Meyer,

and L. Young, Ghost-imaging-enhanced non-invasive spectral characterization of stochastic x-ray free-electron-laser pulses, Commun. Phys. **5**, 191 (2022).

[25] Y. Kayser, C. Milne, P. Juranić, L. Sala, J. Czapla-Masztafiak, R. Follath, M. Kavčič, G. Knopp, J. Rehanek, W. Błachucki *et al.*, Core-level nonlinear spectroscopy triggered by stochastic x-ray pulses, Nat. Commun. **10**, 4761 (2019).

[26] P.-A. Moreau, E. Toninelli, T. Gregory, and M. J. Padgett, Ghost imaging using optical correlations, Laser Photonics Rev. **12**, 1700143 (2018).

[27] A. Schori and S. Shwartz, X-ray ghost imaging with a laboratory source, Opt. Express **25**, 14822 (2017).

[28] Y. Klein, O. Sefi, H. Schwartz, and S. Shwartz, Chemical element mapping by x-ray computational ghost fluorescence, Optica **9**, 63 (2022).

[29] O. Sefi, Y. Klein, E. Strizhevsky, I. P. Dolbnya, and S. Shwartz, X-ray imaging of fast dynamics with single-pixel detector, Opt. Express **28**, 24568 (2020).

[30] Y. Klein, A. Schori, I. P. Dolbnya, K. Sawhney, and S. Shwartz, X-ray computational ghost imaging with single-pixel detector, Opt. Express **27**, 3284 (2019).

[31] D. Pelliccia, A. Rack, M. Scheel, V. Cantelli, and D. M. Paganin, Experimental X-Ray Ghost Imaging, Phys. Rev. Lett. **117**, 113902 (2016).

[32] H. Yu, R. Lu, S. Han, H. Xie, G. Du, T. Xiao, and D. Zhu, Fourier-Transform Ghost Imaging with Hard X Rays, Phys. Rev. Lett. **117**, 113901 (2016).

[33] A. Schori, D. Borodin, K. Tamasaku, and S. Shwartz, Ghost imaging with paired x-ray photons, Phys. Rev. A **97**, 063804 (2018).

[34] Y. Y. Kim, L. Gelisio, G. Mercurio, S. Dziarzhytski, M. Beye, L. Bocklage, A. Classen, C. David, O. Yu. Gorobtsov, R. Khubbutdinov *et al.*, Ghost imaging at an XUV free-electron laser, Phys. Rev. A **101**, 013820 (2020).

[35] D. Ratner, J. P. Cryan, T. J. Lane, S. Li, and G. Stupakov, Pump-Probe Ghost Imaging with SASE FELs, Phys. Rev. X **9**, 011045 (2019).

[36] F. Capotondi, E. Pedersoli, N. Mahne, R. H. Menk, G. Passos, L. Raimondi, C. Svetina, G. Sandrin, M. Zangrando, M. Kiskinova *et al.*, Invited article: Coherent imaging using seeded free-electron laser pulses with variable polarization: First results and research opportunities, Rev. Sci. Instrum. **84**, 051301 (2013).

[37] F. Capotondi, E. Pedersoli, F. Bencivenga, M. Manfredda, N. Mahne, L. Raimondi, C. Svetina, M. Zangrando, A. Demidovich, I. Nikolov *et al.*, Multipurpose end-station for coherent diffraction imaging and scattering at FERMI@Elettra free-electron laser facility, J. Synchrotron Radiat. **22**, 544 (2015).

[38] E. Allaria, D. Castronovo, P. Cinquegrana, P. Craievich, M. Dal Forno, M. B. Danailov, G. D'Auria, A. Demidovich, G. De Ninno, S. Di Mitri *et al.*, Two-stage seeded soft-x-ray free-electron laser, Nat. Photonics **7**, 913 (2013).

[39] G. Penco, E. Allaria, G. De Ninno, E. Ferrari, and L. Giannessi, Experimental Demonstration of Enhanced Self-Amplified Spontaneous Emission by an Optical Klystron, Phys. Rev. Lett. **114**, 013901 (2015).

[40] L. Raimondi, C. Svetina, N. Mahne, D. Cocco, A. Abrami, M. De Marco, C. Fava, S. Gerusina, R. Gobessi, F. Capotondi *et al.*, Microfocusing of the FERMI@Elettra FEL beam with a K-B active optics system: Spot size predictions by application of the WISE code, Nucl. Instrum. Methods Phys. Res., Sect. A **710**, 131 (2013).

[41] R. Sobierajski, I. Jacyna, P. Dłużewski, M. T. Klepka, D. Klinger, J. B. Pełka, T. Burian, V. Hájková, L. Juha, K. Saksl *et al.*, Role of heat accumulation in the multi-shot damage of silicon irradiated with femtosecond XUV pulses at a 1 MHz repetition rate, Opt. Express **24**, 15468 (2016).

[42] D. Gauthier, P. R. Ribič, G. De Ninno, E. Allaria, P. Cinquegrana, M. B. Danailov, A. Demidovich, E. Ferrari, L. Giannessi, B. Mahieu, and G. Penco, Spectrotemporal Shaping of Seeded Free-Electron Laser Pulses, Phys. Rev. Lett. **115**, 114801 (2015).

[43] P. Finetti, H. Höppner, E. Allaria, C. Callegari, F. Capotondi, P. Cinquegrana, M. Coreno, R. Cucini, M. B. Danailov, A. Demidovich *et al.*, Pulse Duration of Seeded Free-Electron Lasers, Phys. Rev. X **7**, 021043 (2017).

[44] S. Nannarone, F. Borgatti, A. DeLuisa, B. P. Doyle, G. C. Gazzadi, A. Giglia, P. Finetti, N. Mahne, L. Pasquali, M. Pedio *et al.*, The BEAR Beamline at Elettra, in *1st International Conference on Achieving the Sustainable Development Goals*, AIP Conf. Proc. No. 705 (AIP, Melville, NY, 2004), p. 450.

[45] C. Li, W. Yin, H. Jiang, and Y. Zhang, An efficient augmented Lagrangian method with applications to total variation minimization, Comput. Optimization Appl. **56**, 507 (2013).

[46] A. Gatti, E. Brambilla, M. Bache, and L. A. Lugiato, Ghost Imaging with Thermal Light: Comparing Entanglement and ClassicalCorrelation, Phys. Rev. Lett. **93**, 093602 (2004).

[47] S. Hofmann, *Auger-and X-Ray Photoelectron Spectroscopy in Materials Science: A User-Oriented Guide* (Springer Science & Business Media, Berlin, 2012).

[48] O. Y. Gorobtsov, G. Mercurio, F. Capotondi, P. Skopintsev, S. Lazarev, I. A. Zaluzhnyy, M. B. Danailov, M. Dell'Angela, M. Manfredda, E. Pedersoli *et al.*, Seeded x-ray free-electron laser generating radiation with laser statistical properties, Nat. Commun. **9**, 4498 (2018).

[49] O. Katz, Y. Bromberg, and Y. Silberberg, Compressive ghost imaging, Appl. Phys. Lett. **95**, 131110 (2009).

[50] S. Krinsky and Y. Li, Statistical analysis of the chaotic optical field from a self-amplified spontaneous-emission free-electron laser, Phys. Rev. E **73**, 066501 (2006).

[51] M. Veronese, R. Appio, P. Craievich, and G. Penco, Absolute Bunch Length Measurement Using Coherent Diffraction Radiation, Phys. Rev. Lett. **110**, 074802 (2013).

[52] S. Krinsky and R. L. Gluckstern, Analysis of statistical correlations and intensity spiking in the self-amplified spontaneous-emission free-electron laser, Phys. Rev. Spec. Top.–Accel. Beams **6**, 050701 (2003).

[53] S. K. Cushing, A. Lee, I. J. Porter, L. M. Carneiro, H.-T. Chang, M. Zürch, and S. R. Leone, Differentiating photoexcited carrier and phonon dynamics in the $\Delta$, $L$, and $\Gamma$ valleys of Si(100) with transient extreme ultraviolet spectroscopy, J. Phys. Chem. C **123**, 3343 (2019).

[54] S. Sastry, Illuminating liquid polymorphism in silicon, PNAS **107**, 17063 (2010).

[55] M. Beye, F. Sorgenfrei, W. F. Schlotter, W. Wurth, and A. Föhlisch, The liquid-liquid phase transition in silicon revealed by snapshots of valence electrons, PNAS **107**, 16772 (2010).